

CrossMark
click for updatesCite this: *J. Mater. Chem. C*, 2015,
3, 10107

Synthesis, luminescence properties, and growth mechanisms of $\text{YF}_3\text{:Yb}^{3+}/\text{Er}^{3+}$ nanoplates†

G. Murali,^a Byeong Hoon Lee,^a R. K. Mishra,^a Jae Myeong Lee,^a Sang-Hwan Nam,^b Yung Doug Suh,^{bc} Dong-Kwon Lim,^{*d} Joong Hee Lee^a and Seung Hee Lee^{*a}

Anisotropically structured upconversion nanocrystals capable of exhibiting bright upconversion emission properties are a promising new class of high performance optical materials. In this study, we investigate a facile synthetic method for the new nanoplate structure of $\text{YF}_3\text{:Yb}^{3+}/\text{Er}^{3+}$ with enhanced luminescence intensity. The shape of $\text{YF}_3\text{:Yb}^{3+}/\text{Er}^{3+}$ nanocrystals can be controlled by changing the synthesis conditions of the NaOH concentration, reaction time, and surfactant. The concentration of NaOH determines the final structure of $\text{YF}_3\text{:Yb}^{3+}/\text{Er}^{3+}$. By increasing the NaOH concentration from 0.25 mmol to 2.5 mmol, $\text{YF}_3\text{:Yb}^{3+}/\text{Er}^{3+}$ nanoplates transform into $\text{NaYF}_4\text{:Yb}^{3+}/\text{Er}^{3+}$ nanoparticles; in the absence of NaOH, the nanoplate structure of $\text{YF}_3\text{:Yb}^{3+}/\text{Er}^{3+}$ changes to particles. The $\text{YF}_3\text{:Yb}^{3+}/\text{Er}^{3+}$ nanoplates show luminescence efficiency much greater than that of the spherical $\text{YF}_3\text{:Yb}^{3+}/\text{Er}^{3+}$ nanocrystals.

Received 7th July 2015,
Accepted 4th September 2015

DOI: 10.1039/c5tc02034d

www.rsc.org/MaterialsC

1. Introduction

Recently, lanthanide (Ln^{3+})-doped upconversion nanoparticles (UCNPs) have attracted special attention because of their ability to convert low-energy near-infrared (NIR) photons into high-energy visible emissions *via* multiple absorptions or energy transfers.¹ The emission characteristics of UCNPs, such as the wavelength and intensity, strongly depend on the host lattice, types of dopants and co-dopants, and overall structural parameters such as the size, shape, and crystallographic phase.² Therefore, the precise control of nanocrystals' size and morphology is vital to permit the fine control of UCNPs' optical properties. So far, various synthetic approaches including solvo/hydrothermal synthesis, Ostwald ripening, sol-gel processes, thermal decomposition, co-precipitation, and ionic-liquid-based syntheses have been investigated to obtain finely controlled UCNPs of specific shapes.³ All these methods have revealed that the shape of UCNPs depends not only on the intrinsic structure of the host lattice but also on synthetic parameters such as solvents, surfactants,

reaction temperature and time, and precursor compositions. In particular, organic surfactants capable of selective binding to certain crystal facets and suppression of their growth rates are crucial for controlling the morphology of UCNPs. Oleic acid (OA) or a combination of OA and oleylamine (OM) has been the most widely used to control the size and shape of UCNPs; OM alone has not been a popular surfactant, as it produces irregular morphologies. The presence of inorganic species in the reaction mixture has been demonstrated to be effective in controlling the phase and morphology of UCNPs.⁴

Host lattices including oxides, fluorides, phosphates, oxyhalides, oxysulfides, and vanadates have been investigated for upconversion (UC) luminescence through lanthanide doping.⁵ Substantial effort has been devoted to the fabrication of fluoride-based UCNPs because of their high quantum yields and chemical stability, which may allow them to provide the highest UC efficiency.⁶ Among all fluorides, NaYF_4 has been reported to be the best host material; the UC efficiency of NaYF_4 with $\text{Yb}^{3+}/\text{Er}^{3+}$ ion pairs has been reported to be particularly high, because Er^{3+} has two successive pairs of energy levels ($^4\text{I}_{11/2}$ and $^4\text{I}_{15/2}$ states; $^4\text{I}_{11/2}$ and $^4\text{F}_{7/2}$ states) with similar energy gaps of approximately $10\,350\text{ cm}^{-1}$ (1.28 eV).⁷

The fluoride host material YF_3 has recently received much attention for its strong photoluminescence (PL) properties.⁸ The UC efficiency of bulk YF_3 was reported to exceed that of hexagonal NaYF_4 with $\text{Yb}^{3+}/\text{Er}^{3+}$ or $\text{Yb}^{3+}/\text{Tm}^{3+}$ doping.⁹ Further, Wang *et al.*¹⁰ reported that the UC emission intensity of $\text{YF}_3\text{:Yb}^{3+}/\text{Er}^{3+}$ nanocrystals exceeded that of $\text{CaF}_2\text{:Yb}^{3+}/\text{Er}^{3+}$ and $\text{NaYF}_4\text{:Yb}^{3+}/\text{Er}^{3+}$ nanocrystals. These studies demonstrated the usefulness of YF_3 over NaYF_4 to realize high UC efficiency. Because of the strong dependence of UCNPs' optical properties

^a Applied Materials Institute for BIN Convergence, Department of BIN Fusion Technology and Department of Polymer-Nano Science and Technology, Chonbuk National University, Jeonju, Jeonbuk 561-756, Korea.
E-mail: lsh1@chonbuk.ac.kr; Tel: +82-63-270-2343

^b Laboratory for Advanced Molecular Probing (LAMP), Korea Research Institute of Chemical Technology, Daejeon 305-600, South Korea

^c School of Chemical Engineering, Sungkyunkwan University, Suwon 440-746, South Korea

^d KU-KIST Graduate School of Converging Science and Technology, Korea University, 145 Anam-ro, Seongbuk-gu, Seoul, 136-701, Korea.
E-mail: dklm@korea.ac.kr

† Electronic supplementary information (ESI) available. See DOI: 10.1039/c5tc02034d

on their morphologies, researchers have attempted tailoring the morphology of YF_3 by changing the solvent ratio or precursor ratio.¹¹ However, most of these studies focused on single-lanthanide-ion-doped YF_3 nanocrystals. Morphology control and UC emissions with a range of sensitizer and activator ions co-doped into YF_3 nanocrystals have not yet been widely investigated.

Herein, we report a new $\text{YF}_3:\text{Yb}^{3+}/\text{Er}^{3+}$ structure of nanoplates, prepared by a simple synthetic method, using mixed solvent compositions (oleylamine (OM) and 1-octadecene (ODE)) in the presence of NaOH. The morphology and crystalline phase of the nanoplate depend strongly on the presence and amount of NaOH. When the NaOH concentration increased from 0.25 mmol (0.01 g) to 2.5 mmol (0.1 g), the nanocrystals transformed from the pure octahedral-phase YF_3 nanoplate structure to pure cubic-phase NaYF_4 nanoparticles. The nanoplate structures of $\text{YF}_3:\text{Yb}^{3+}/\text{Er}^{3+}$ showed strong UC PL intensity compared to the spherical $\text{YF}_3:\text{Yb}^{3+}/\text{Er}^{3+}$ and $\text{NaYF}_4:\text{Yb}^{3+}/\text{Er}^{3+}$ nanoparticle structures. Detailed reaction conditions were investigated and a plausible growth mechanism was proposed.

2. Experimental section

2.1 Materials

$\text{YCl}_3 \cdot 6\text{H}_2\text{O}$, $\text{YbCl}_3 \cdot 6\text{H}_2\text{O}$, $\text{ErCl}_3 \cdot 6\text{H}_2\text{O}$, NH_4F , NaOH, ODE, OM, OA, and trioctylphosphine (TOP) were purchased from Sigma-Aldrich (St. Louis, MO). All chemicals were used as received without further purification.

2.2 Typical synthetic procedures for $\text{YF}_3:\text{Yb}^{3+}/\text{Er}^{3+}$ nanoplates

Briefly, $\text{YCl}_3 \cdot 6\text{H}_2\text{O}$ (0.1562 g, 0.51 mmol), $\text{YbCl}_3 \cdot 6\text{H}_2\text{O}$ (0.0503 g, 0.13 mmol), and $\text{ErCl}_3 \cdot 6\text{H}_2\text{O}$ (0.0055 g, 0.014 mmol) were mixed with 3 mL of OM and 17 mL of ODE in a 50 mL round-bottom Pyrex flask under continuous stirring. The mixture was heated to 160 °C to homogenize the solution and maintained at this temperature for 30 min. The mixture was then cooled to room temperature (25 °C) and 10 mL of methanol solution containing NaOH (0.01 g, 0.25 mmol) and NH_4F (0.148 g, 4 mmol) was added dropwise. The mixed solution was stirred for 30 min. Then the solution was heated to 120 °C and maintained at this temperature for 15 min to remove excess methanol. Subsequently, the solution was heated to 310 °C and maintained at this temperature for 2 h under Ar. Afterward, the solution was naturally cooled to room temperature (25 °C) under Ar; the nanocrystals were precipitated by centrifugation (15 000 rpm, 15 min). Finally, the precipitates were washed twice with ethanol/water (1:1 v/v) and dispersed in ethanol.

2.3 Characterization

The crystallinity of the nanostructures was determined by X-ray powder diffraction (XRD) using a MAX-2500 instrument and Fe-filtered $\text{Cu-K}\alpha$ radiation ($\lambda = 1.54 \text{ \AA}$). The morphologies and microstructures of the products were characterized by high-resolution transmission electron microscopy (HRTEM) (HITACHI H-7650 and JEOL JEM-2010) and field emission scanning electron

microscopy (FESEM) (HITACHI SU-70). Elemental mapping analysis of the samples was performed using field emission energy-filtering transmission electron microscopy (FETEM) (JEM-2200FS) to obtain the elemental distributions of the nanostructures. Fluorescence spectra were recorded using a home-made microscope equipped with a spectrometer and a near-infrared (NIR) laser (980 nm).

3. Results and discussion

3.1 Structural and morphological studies

X-ray diffraction analysis (XRD) of the product obtained from typical synthetic procedures shows the crystalline structure of $\text{YF}_3:\text{Yb}^{3+}/\text{Er}^{3+}$, which is well-matched with that of YF_3 's pure orthorhombic phase (JCPDS No. 74-0911) (Fig. 1). However, the peak corresponding to the (020) lattice plane shows significantly higher intensity compared with that of orthorhombic YF_3 . This peak is believed to arise from the lattice plane perpendicular to the (020) plane, which is more prevalent than those of other crystal directions in the obtained nanostructures.

The TEM and FESEM images of the as-prepared $\text{YF}_3:\text{Yb}^{3+}/\text{Er}^{3+}$ nanocrystal show the dominant formation of rectangular nanoplate structures with lengths of 160–240 nm, widths of 70–140 nm, and thicknesses of 13–17 nm (Fig. 2(a)–(d) and Fig. S1 in the ESI[†]). The rectangular nanoplates appear to taper from both sides at the middle, as the width of the nanoplate decreases from the ends to the center (Fig. 2(c)). The nanoplates' thicknesses are not uniform, as observed by the contrast difference in the nanoplate structure in the TEM images (red dotted line in Fig. 2(c)). The thicker portion in the nanoplate resembles scissors in shape. Interestingly, the magnified view in Fig. 2(d) shows the same embedded scissor structure in the nanoplate, which indicates a possible growth mechanism. The scissor-shape nanostructures are visible in the TEM images in Fig. 2(b). While the majority of the structure is the nanoplate, the as-prepared sample also comprises several other structures,

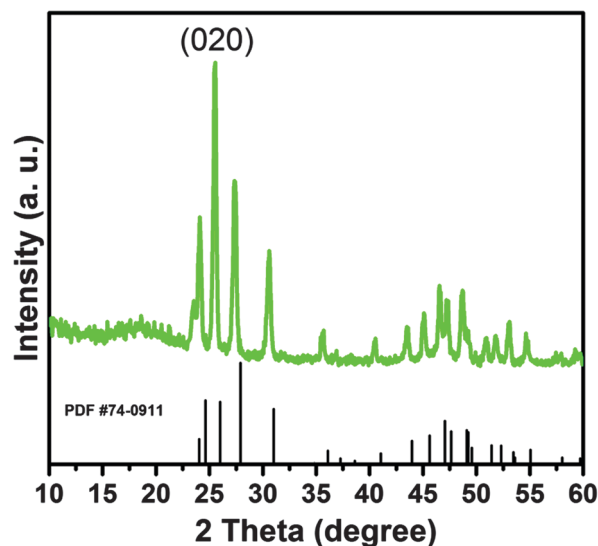


Fig. 1 XRD pattern of the $\text{YF}_3:\text{Yb}^{3+}/\text{Er}^{3+}$ nanoplate structure.

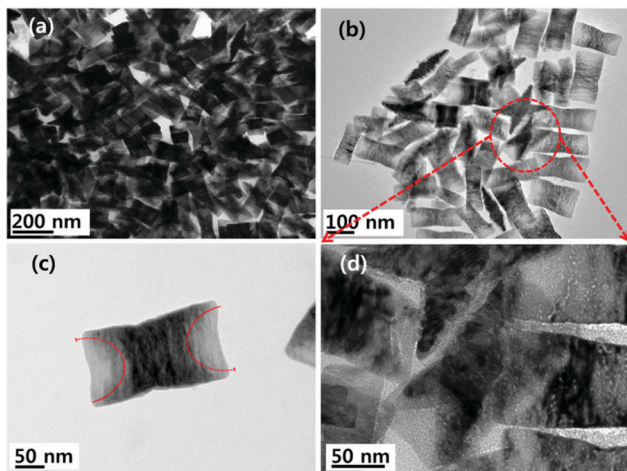


Fig. 2 TEM images of $\text{YF}_3:\text{Yb}^{3+}/\text{Er}^{3+}$ nanoplates.

including monopods, tripods, tetrapods, pentapods, hexapods, and highly branched structures, possibly as intermediate structures for the formation of nanoplates (Fig. 3 and Fig. S2–S4, ESI†). The dark-field FETEM image of nanoplates clearly shows contrast differences at both ends of the nanoplates (Fig. 4(a)). Elemental mapping of nanoplates for Y, F, Yb, and Er shows a uniform distribution of each element throughout the nanoplate structure without specific areal localization (Fig. 4(b)). Though the quantity of activator Er^{3+} is very low, the species' presence in the nanoplate is evident from the energy-dispersive X-ray analysis (EDX) spectra shown in (Fig. 4(c)).

The edges of the dark regions in the nanoplate structure show a crystalline nature with interplanar distances of 0.33 nm and 0.36 nm, corresponding to the [200] and [101] lattice planes of YF_3 , respectively (Fig. 5(a) and (b)). The measured angle between the [200] and [101] planes is 55° , based on HRTEM, which exactly matches the angle of a typical orthorhombic crystal structure. The symmetric SAED pattern shown in Fig. 5(c) indicates the crystalline state of the nanoplate. Based on HRTEM and SAED pattern analysis, the crystal growth of the nanoplate preferentially occurs in the [002] direction on the flat exposed [010] surface, in good agreement with the XRD results in Fig. 1. The lattice plane of both end parts of the nanoplate, corresponding to the lighter part in

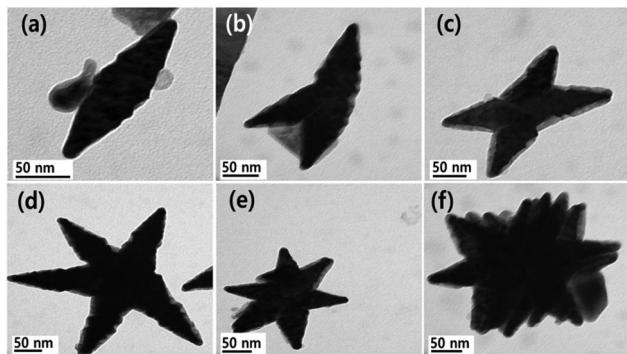


Fig. 3 TEM images of $\text{YF}_3:\text{Yb}^{3+}/\text{Er}^{3+}$ (a) monopod (b) tripod (c) tetrapod (d) pentapod (e) hexapod and (f) hierarchical structures.

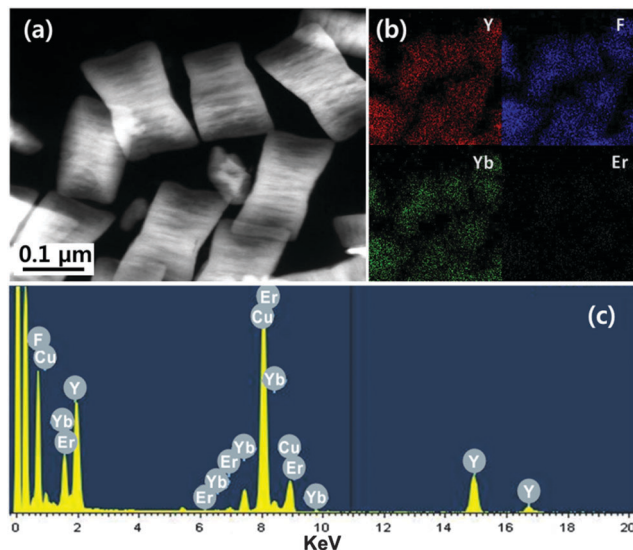


Fig. 4 (a) Dark-field FETEM image, (b) elemental mapping for Y, F, Yb, and Er, and (c) EDX spectrum of $\text{YF}_3:\text{Yb}^{3+}/\text{Er}^{3+}$ nanoplates.

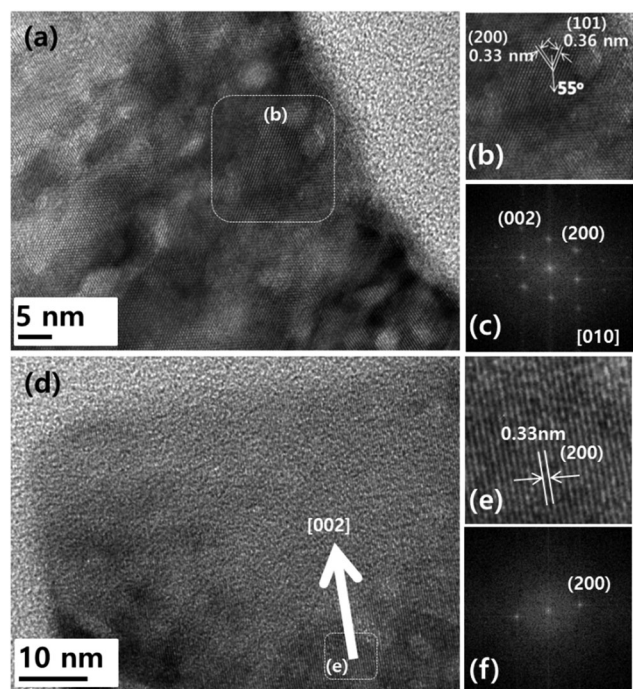


Fig. 5 (a) HRTEM, (b) magnified HRTEM, and (c) SAED images of $\text{YF}_3:\text{Yb}^{3+}/\text{Er}^{3+}$ nanoplates. (d) HRTEM, (e) magnified HRTEM, and (f) SAED images of the end portion of the nanoplate.

Fig. 2(c) and the dark part in Fig. 4(a), is the dominant crystal lattice plane of [200] (Fig. 5(d)–(f)). These results indicate that the backbones of the nanoplate are composed of mixtures of two different lattice planes (*i.e.*, [200] and [101]) and the other part of the nanoplate was dominantly filled with [200] lattice planes.

3.2 Reaction parameters for nanoplate morphology

The morphology of UC nanoparticles is strongly dependent on the experimental parameters. We investigated the reaction

parameters of NaOH concentration, reaction time, and surfactant composition.

3.2.1 NaOH concentration. The effects of NaOH concentration on the crystal structures and morphological evolution processes of the $\text{YF}_3\text{:Yb}^{3+}/\text{Er}^{3+}$ nanoplates were investigated by changing the concentration of NaOH from 0 to 2.5 mmol while maintaining other experimental conditions at fixed values. The XRD patterns of samples prepared using different NaOH concentrations (0, 0.25, 0.75, 1.25, 1.75, 2.25, and 2.5 mmol) are shown in Fig. 6(a). As the NaOH concentration increases to 2.5 mmol, the structure and composition of the samples transform from orthorhombic YF_3 to cubic NaYF_4 . TEM images of samples prepared without and with 2.5 mmol NaOH concentrations are shown in Fig. 6(b)–(e). From the TEM images, NaOH concentration is clearly observed to be crucial for the formation of the nanoplate morphology. If either 0 or 2.5 mmol of NaOH is used, nanoparticles result instead of nanoplates (Fig. 6(b)–(d)). The HRTEM and SAED images of the sample prepared without

NaOH, shown in Fig. 6(c), indicate that the particles consist of orthorhombic single-crystalline YF_3 . Meanwhile, the particles prepared using 2.5 mmol of NaOH show 0.28 nm spacing in the HRTEM image, corresponding to the [200] plane of cubic NaYF_4 (Fig. 6(e)). The elemental mapping analysis of $\text{NaYF}_4\text{:Yb}^{3+}/\text{Er}^{3+}$ shows uniform distribution of elemental Na, Y, F, Yb, and Er in the particles (Fig. S5, ESI[†]). However, the use of NaOH concentrations between 0.25 and 1.75 mmol produces mixtures of nanoparticles and nanoplates (Fig. S6, ESI[†]). The amount of spherical particle structure in the mixtures is proportional to the concentration of NaOH; the nanoplate structure disappears entirely at a NaOH concentration of 2.25 mmol. The structural transformation from orthorhombic YF_3 to cubic NaYF_4 begins at this NaOH concentration, as well. These results demonstrate the critical role of NaOH concentration in obtaining the nanoplate structure. When increasing the concentration of NaOH from 0 to 2.5 mmol, the host matrix for the Yb and Er dopant species changes from YF_3 to NaYF_4 , and the morphology of the nanostructure also changes from particle to nanoplate to particle again.

3.2.2 Reaction time. We investigated the effect of reaction time on the crystal structures and morphologies of the nanoplates (Fig. 7 and Fig. S7 and S8, ESI[†]). The XRD patterns of the products obtained at 310 °C for 30 min and 1 h are both displayed in Fig. 7. The XRD pattern of the product obtained after 30 min cannot be indexed as YF_3 or other Y compounds. As shown in Fig. 7(b) and (c), the product morphology contained predominantly small particles with a small amount of rod-shaped particles. The XRD of the product obtained after 1 h shows a pattern well-matched with that of orthorhombic YF_3 . The dominant structure within this product is nanoplates, as shown in Fig. 7(d) and (e). Hence, the minimum reaction time to obtain the desired $\text{YF}_3\text{:Yb}^{3+}/\text{Er}^{3+}$ nanoplate structure is 1 h; the nanoplate structures are produced by a change in the shapes of particle structures.

3.2.3 Composition of surfactants. The effect of surfactant composition on the resulting nanostructure was investigated using the three surfactant compositions of 100% OA, a 1:1 mixture of OM and OA, and a 1:1 mixture of OM and TOP. Fig. S9 (ESI[†]) shows the XRD patterns of the $\text{Yb}^{3+}/\text{Er}^{3+}$ -doped YF_3 nanocrystals obtained using the three surfactants. Clearly, the formation of the pure cubic phase dominates for nanocrystals prepared using the OM/TOP mixture; all peaks are well-indexed to those of standard cubic YF_3 (ICSD PDF Card No. 01-072-0579) (Fig. S9, ESI[†]). For OA and the OM/OA mixture, mixtures of orthorhombic and cubic phases form, as shown in Fig. S9 (ESI[†]). The sample prepared using the OA/OM mixture shows the dominant formation of standard cubic YF_3 . Importantly, the nanocrystal shapes in the different solvent compositions are poorly developed in all cases, with no nanoplate or nanopod structures (Fig. S10, ESI[†]). Only irregular and clustered particles appear. Hence, the suitability of OM for nanoplate preparation is supported.

3.3 Fluorescence properties

The PL properties of all nanocrystals were investigated with excitation from a 980 nm laser. As shown in Fig. 8, nanocrystals

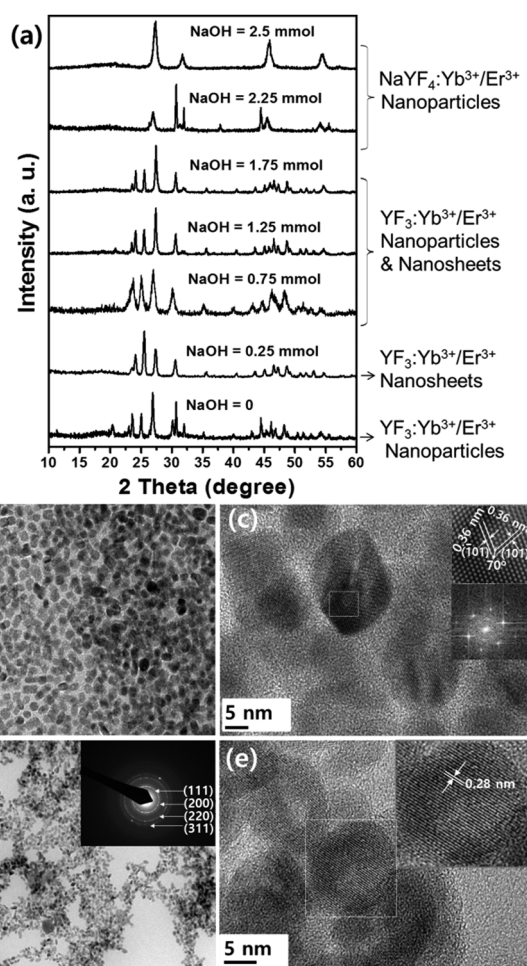


Fig. 6 (a) XRD patterns of samples prepared using different NaOH concentrations. TEM images of (b and c) $\text{YF}_3\text{:Yb}^{3+}/\text{Er}^{3+}$ nanoparticles (without NaOH) and (d and e) $\text{NaYF}_4\text{:Yb}^{3+}/\text{Er}^{3+}$ nanoparticles (2.5 mmol NaOH). Insets in panel (c), from top to bottom, are an HRTEM image and the corresponding SAED pattern, respectively, of a particle. The inset in panel (d) is the SAED pattern of the particles; the inset in panel (e) is the HRTEM image of a particle.

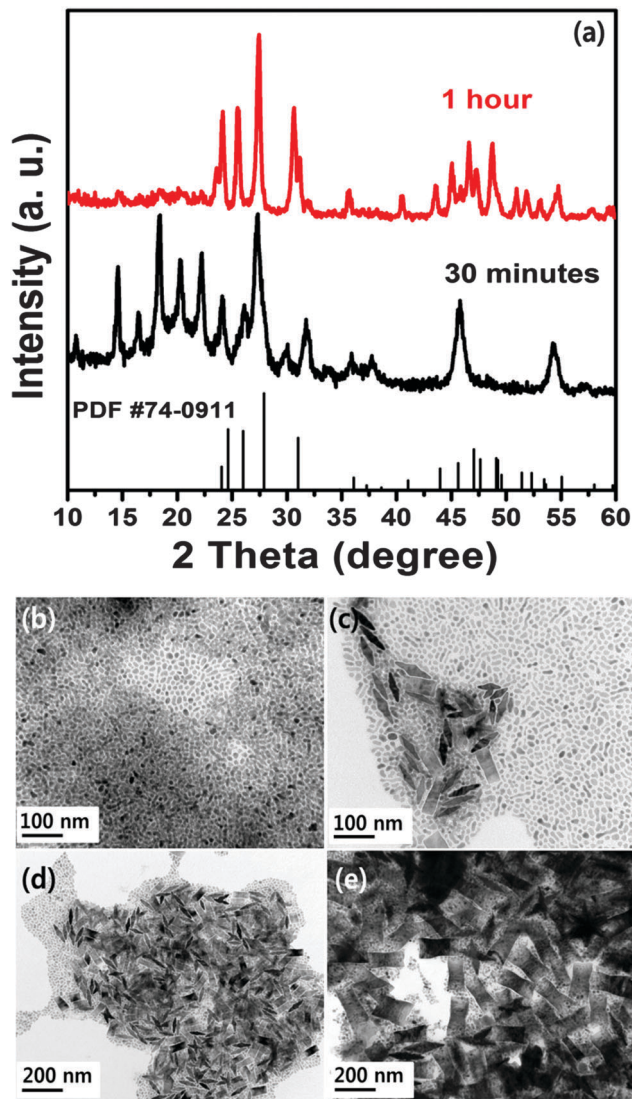


Fig. 7 (a) XRD patterns of samples obtained at different reaction times. TEM images of samples reacted for (b and c) 30 min and (d and e) 1 h.

prepared using different reaction times and using different NaOH concentrations show the characteristic green and red UC emission spectrum, with strong emissions of 650–670 nm and a weak 550 nm emission.

Interestingly, the PL intensity of the nanocrystals shows strong structural dependence, as shown in Fig. 8(a). The PL intensities of nanoplates or nanoplate/nanoparticle mixtures of $\text{YF}_3:\text{Yb}^{3+}/\text{Er}^{3+}$ are clearly observed to be stronger than those of particles of either $\text{YF}_3:\text{Yb}^{3+}/\text{Er}^{3+}$ (prepared without NaOH) or $\text{NaYF}_4:\text{Yb}^{3+}/\text{Er}^{3+}$ (prepared using 2.5 mmol of NaOH). NaYF_4 nanoparticles show higher PL intensity than $\text{YF}_3:\text{Yb}^{3+}/\text{Er}^{3+}$ nanoparticles, which can be attributed to the host matrix effect. The PL intensities of $\text{YF}_3:\text{Yb}^{3+}/\text{Er}^{3+}$ nanoplates are 2.3 and 1.7 times higher for red and green emission, respectively, compared with those of $\text{NaYF}_4:\text{Yb}^{3+}/\text{Er}^{3+}$ nanoparticles. The higher PL intensity of $\text{YF}_3:\text{Yb}^{3+}/\text{Er}^{3+}$ nanoplates/nanoparticles compared with that of $\text{YF}_3:\text{Yb}^{3+}/\text{Er}^{3+}$ nanoparticles could be attributed to the combined influence of morphology and particle size. As we know,

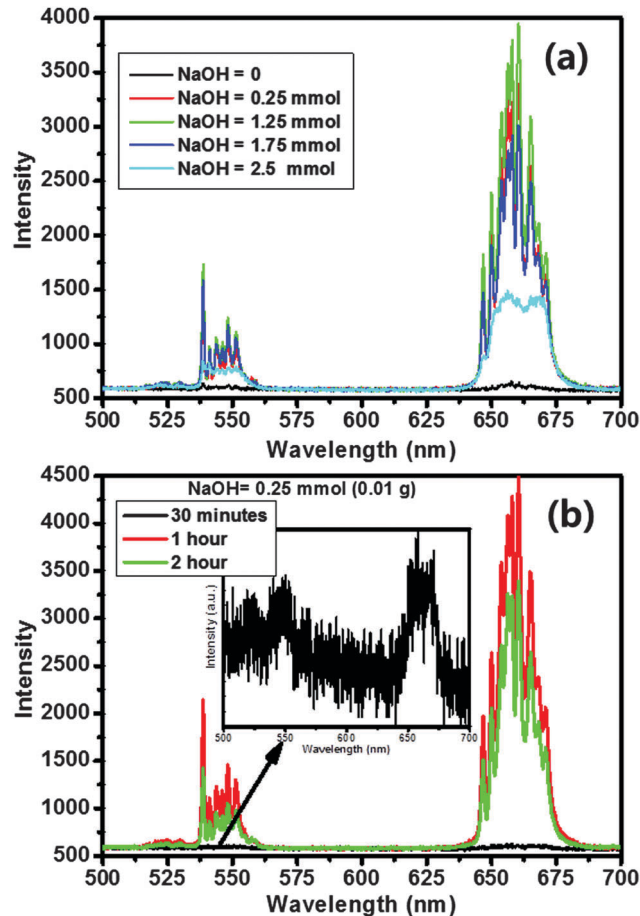


Fig. 8 PL spectra of samples prepared (a) using different NaOH concentrations and (b) using different reaction times (0.25 mmol of NaOH). The samples were excited at 980 nm with a 360 mW diode laser.

each peak in the emission spectrum is contributed by the transitions of dopant ions in the interior and at the surface of the nanostructures. Because of surfactants and surface defects on the surface of the nanostructures, compared to interior ions, the surface ions contribute very weak emission to the actual emission. Since the density of surface defects increases with decreasing particle size, $\text{YF}_3:\text{Yb}^{3+}/\text{Er}^{3+}$ nanoparticles will maintain a higher density of volume defects, contributing to weak UC luminescence intensity. When the morphology changes from nanoparticles to rectangular nanoplates *via* rhombic nanoplate morphology, the concentration of the surface dopant ions decreases, leading to an increase in the relative emission intensity.¹² Upconversion luminescence photographs of as-prepared nanostructures under 980 nm excitation are shown in Fig. S11 (ESI[†]). In the case of $\text{YF}_3:\text{Yb}^{3+}/\text{Er}^{3+}$ nanoplates, it showed strong yellow colour emission because of the sharp green and red emissions (shown in Fig. 8(a)). However, when the host lattice changes from YF_3 to NaYF_4 , the emission colour changes from yellow to green as shown in Fig. S11 (ESI[†]).

Because the reaction time can greatly influence the resulting nanostructure, as shown in Fig. 7, variations in PL intensity according to the products' reaction times are shown in Fig. 8(b). Nanoparticles obtained after 30 min show very low PL intensity

because of the poor or undeveloped crystalline structure of the particles' host matrices. However, nanoparticles obtained after 1 h and 2 h both exhibit high PL intensity.

PL studies were also performed for samples prepared using different surfactants (Fig. S12, ESI†). Nanoparticles prepared using OA and mixed OA/OM as a surfactant show very weak emission properties. The efficiency of PL emission is known to depend on the local environment, including factors such as site symmetry and the crystal-field strength of rare-earth dopant species. The weak emission can be attributed to the poor development of the samples' crystalline phases, which distorts the crystal symmetry and dissipates the excitation energy of the dopant ions. Samples prepared using an OM/TOP surfactant, which contain pure cubic YF_3 , produce higher PL intensity. However, the emission intensity of the cubic YF_3 particles is very low compared to that of either cubic NaYF_4 particles or orthorhombic YF_3 nanoplates and nanoparticles.

3.4 Growth mechanism of nanoplates

Structural and morphological observations of samples prepared under different reaction conditions indicated that reaction time, NaOH concentration, and surfactant composition all greatly influence the morphology of YF_3 particles. A specific NaOH concentration and surfactant were found to be necessary for the formation of nanoplate structures. The released Na^+ from NaOH is assumed to have dual functions. Selective adsorption of Na^+ and OM molecules onto different facets of growing YF_3 crystals, resulting from strong interactions between these cations and the fluoride anions on the particle surface, causes the formation of unique nanostructures. The Na^+ ions can also enter into YF_3 's crystal structure, causing structural transformations.

As the reaction temperature increases to 310 °C, reagents present in the reaction medium of NH_4F , NaOH, and $\text{RECl}_3 \cdot 6\text{H}_2\text{O}$ begin to dissociate into NH_4^+ , F^- , Na^+ , OH^- , RE^{3+} , and Cl^- ions, in which the rare earth (RE) species here are Y, Yb, and Er. Na^+ , Y^{3+} , and F^- become surrounded by the oppositely charged OH^- , Cl^- , and NH_4^+ as a result of electrostatic interactions. This decreases collisions between Na^+ , Y^{3+} , and F^- , reducing the nucleation rate of crystallites. At lower concentrations of NaOH, YF_3 crystallites are free to form because of the weaker competition between Na^+ and Y^{3+} ; free Na^+ , together with oleylamine, become selectively adsorbed on the surface of denser atoms. Na^+ and organic additives retain their influence on the shape-controlled crystal growth, selectively modifying the growth of different facets of the YF_3 crystal and driving the formation of nanopod structures with tips in the [002] growth direction. TEM images indicate that $\text{YF}_3:\text{Yb}^{3+}/\text{Er}^{3+}$ nanoplates may form through a "two-step formation mechanism", where secondary nanostructures grow from primary nanostructures to determine the final morphology. The proposed growth mechanism of the nanoplates is shown in Fig. 9. In the secondary growth stage, oriented attachments induce the spontaneous attachment of newly produced nuclei to primarily-formed monopods, with easy axes as their preferential growth direction. The growing nanopod continues to grow on both sides of its backbone, resulting in the formation of scissor-like structures, in which

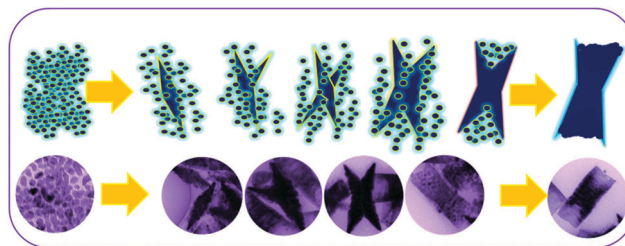


Fig. 9 Schematic of the proposed growth mechanism for $\text{YF}_3:\text{Yb}^{3+}/\text{Er}^{3+}$ nanoplates.

adjacent nanopods share common crystallographic axes. After the formation of scissor-like tetrapods, the nanopods become fused together with a preferred crystallographic orientation that minimizes the structure's surface energy.¹³ The interspace between nanopods then fills with newly produced nuclei, resulting in nanoplates. The planar filling of the interspaces can be attributed to the selective attachment of growing nuclei to the concave corner sites between tetrapod branches, as oriented attachment thermodynamically favored to eliminate the high-energy surfaces of nanocrystals.

As the NaOH concentration increases, the level of supersaturated Na^+ increases; Na^+ begins to diffuse into the crystal lattice of primarily-formed YF_3 particles. For each newly introduced Na^+ ion, an extra F^- is required to establish charge balance. The introduction of F^- into the grain surface may induce transient electric dipoles with their negative poles facing outward. These transient dipoles hamper the growth of YF_3 by electrostatically resisting the diffusion of the growth-required F^- from the solution into the grain, which results in irregularly shaped particles.¹⁴ Hence, by increasing the number of Na^+ ions introduced into the lattice, the number of irregular particles formed increases. At the NaOH concentration of 2.5 mmol, a large amount of Na^+ is introduced into the crystal structure; the electron cloud of the ions becomes distorted from the steric effect caused by the insertion of Na^+ into the crystal lattice.¹⁵ Y^{3+} ions no longer coordinate with the same number of F^- ions and the misbalance of the orthorhombic-phase YF_3 induces the transformation of orthorhombic YF_3 to cubic NaYF_4 . Notably, however, these growth and structural transformation mechanisms are speculations based on the experimental results.

4. Conclusions

Herein, we reported on the fabrication of a new nanoplate structure of $\text{YF}_3:\text{Yb}^{3+}/\text{Er}^{3+}$, using simple reactions with precursors and the tuning of specific reaction parameters, such as NaOH concentration, reaction time, and surfactant composition. The use of NaOH at concentrations exceeding 0.25 mmol and limiting the reaction time to less than 1 h produced spherical $\text{YF}_3:\text{Yb}^{3+}/\text{Er}^{3+}$ nanoparticles, which showed low PL intensity. Experimental results suggested that the formation of nanoplate structures depended greatly on NaOH concentration, reaction time, and surfactant composition. TEM analysis of the intermediate structures suggested that the $\text{YF}_3:\text{Yb}^{3+}/\text{Er}^{3+}$

nanoplates originated from the gradual changes of spherical nanoparticles into anisotropic monopods, scissor-like structures, and finally nanoplates. The $\text{YF}_3:\text{Yb}^{3+}/\text{Er}^{3+}$ nanoplates showed higher PL intensity compared to spherical nanoparticles of either $\text{YF}_3:\text{Yb}^{3+}/\text{Er}^{3+}$ or $\text{NaYF}_4:\text{Yb}^{3+}/\text{Er}^{3+}$. The high PL intensity of $\text{YF}_3:\text{Yb}^{3+}/\text{Er}^{3+}$ nanoplates could potentially be utilized in bio-medical imaging,¹⁶ display applications,¹⁷ and efficient energy harvesting.¹⁸ Furthermore, the synthesis method and the increased understanding of the formation of anisotropic UCNPs may provide new insight into the design of new and versatile high-performance optical materials.

Acknowledgements

This research was supported by the National Research Foundation of Korea (NRF) funded by the Ministry of Education (NRF-2013R1A1A1061387), KU-KIST research fund, Basic Science Research Program (2014R1A4A1008140) funded by the Ministry of Science, ICT & Future Planning and Polymer Materials Fusion Research Center.

Notes and references

- X. Li, F. Zhang and D. Zhao, *Nano Today*, 2013, **8**, 643–676.
- O. Ehlert, R. Thomann, M. Darbandi and T. Nann, *ACS Nano*, 2008, **2**(1), 120–124; K. Teshima, S. Lee, N. Shikine, T. Wakabayashi, K. Yubuta, T. Shishido and S. Oishi, *Cryst. Growth Des.*, 2011, **11**, 995–999; Y. Sun, Y. Chen, L. Tian, Y. Yu, X. Kong, J. Zhao and H. Zhang, *Nanotechnology*, 2007, **18**, 275609; C. Li, J. Yang, Z. Quan, P. Yang, D. Kong and J. Lin, *Chem. Mater.*, 2007, **19**, 4933–4942; J. Shan, M. Uddi, R. Wei, N. Yao and Y. Ju, *J. Phys. Chem. C*, 2010, **114**, 2452–2461; D. Yuan, M. C. Tan, R. E. Riman and G. M. Chow, *J. Phys. Chem. C*, 2013, **117**, 13297–13304; F. Wang, R. Deng, J. Wang, Q. Wang, Y. Han, H. Zhu, X. Chen and X. Liu, *Nat. Mater.*, 2011, **10**, 968–973.
- G. Chen, H. Qiu, P. N. Prasad and X. Chen, *Chem. Rev.*, 2014, **114**, 5161–5214.
- L. W. Yang, Y. Li, Y. C. Li, J. J. Li, J. H. Hao, J. X. Zhonga and P. K. Chu, *J. Mater. Chem.*, 2012, **22**, 2254–2262; Q. Zhao, W. Lü, N. Guo, Y. Jia, W. Lv, B. Shao, M. Jiaoa and H. You, *Dalton Trans.*, 2013, **42**, 6902–6908.
- F. Vetrone, J. C. Boyer, J. A. Capobianco, A. Speghini and M. Bettinelli, *J. Appl. Phys.*, 2004, **96**, 661; H. Q. Liu, L. L. Wang and S. Chen, *Mater. Lett.*, 2007, **61**, 3629–3631; C. Li, P. Ma, P. Yang, Z. Xu, G. Li, D. Yang, C. Peng and J. Lin, *CrystEngComm*, 2011, **13**, 1003–1013; R. Lisiecki, W. R. Romanowski, A. Speghini and M. Bettinelli, *J. Lumin.*, 2009, **129**, 521–525; Z. Li, L. Zheng, L. Zhang and L. Xiong, *J. Lumin.*, 2007, **126**, 481–486; A. M. Pires, O. A. Serra and M. R. Davolos, *J. Alloys Compd.*, 2004, **374**, 181–184; T. Tsuboi, *Phys. Rev. B: Condens. Matter Mater. Phys.*, 2000, **62**, 0163–1829; S. Gai, C. Li, P. Yang and J. Lin, *Chem. Rev.*, 2014, **114**, 2343–2389; G. Yang, S. Gai, F. Qu and P. Yang, *ACS Appl. Mater. Interfaces*, 2013, **5**, 5788–5796; R. Lv, P. Yang, F. He, S. Gai, G. Yang and J. Lin, *Chem. Mater.*, 2015, **27**, 483–496; R. Lv, P. Yang, F. He, S. Gai, C. Li, Y. Dai, G. Yang and J. Lin, *ACS Nano*, 2015, **9**(2), 1630–1647.
- S. Zeng, G. Ren, C. Xuab and Q. Yang, *CrystEngComm*, 2011, **13**, 1384–1390; F. Zhang, J. Li, J. Shan, L. Xu and D. Zhao, *Chem. – Eur. J.*, 2009, **15**, 11010–11019.
- X. Zhang, P. Yang, C. Li, D. Wang, J. Xu, S. Gai and J. Lin, *Chem. Commun.*, 2011, **47**, 12143–12145; H. Q. Wang and T. Nann, *ACS Nano*, 2009, **3**(11), 3804–3808.
- L. Li, Y. Yang, R. Fan, Y. Jiang, L. Wei, Y. Shi, J. Yu, S. Chen, P. Wang, B. Yang and W. Cao, *J. Power Sources*, 2014, **264**, 254–261; G. Chen, H. Qiu, R. Fan, S. Hao, S. Tan, C. Yang and G. Han, *J. Mater. Chem.*, 2012, **22**, 20190–20196; C. Wen, L. Sun, J. Yan, Y. Liu, J. Song, Y. Zhang, H. Lian and Z. Kang, *J. Colloid Interface Sci.*, 2011, **357**, 116–120; C. Li, Y. Mei, J. Xie, W. Dai, G. Du and Z. Li, *J. Alloys Compd.*, 2013, **560**, 10–14.
- F. Auzel and D. Pecile, *J. Lumin.*, 1976, **11**, 321; F. Auzel and D. Pecile, *J. Lumin.*, 1973, **8**, 32; F. Auzel, *Chem. Rev.*, 2004, **104**, 139.
- G. Wang, Q. Peng and Y. Li, *J. Am. Chem. Soc.*, 2009, **131**, 14200.
- S. Sarkar and V. Mahalingam, *CrystEngComm*, 2013, **15**, 5750–5755; B. Shao, Q. Zhao, N. Guo, Y. Jia, W. Lv, M. Jiao, W. Lu and H. You, *Cryst. Growth Des.*, 2013, **13**, 3582–3587; Z. Fu, X. Cui, S. Cui, X. Qi, S. Zhou, S. Zhang and J. H. Jeong, *CrystEngComm*, 2012, **14**, 3915–3922; X. Xue, L. Wang, L. Huang, D. Zhao and W. Qin, *CrystEngComm*, 2013, **15**, 2897–2903.
- F. Wang, J. Wang and X. Liu, *Angew. Chem., Int. Ed.*, 2010, **49**, 7456–7460.
- Z. Li, C. Li, Y. Mei, L. Wang, G. Du and Y. Xiong, *Nanoscale*, 2013, **5**, 3030–3036.
- D. Chen, Y. Yu, F. Huang, P. Huang, A. Yang and Y. Wang, *J. Am. Chem. Soc.*, 2010, **132**, 9976–9978; D. Chen, Y. Yu, F. Huang and Y. Wang, *Chem. Commun.*, 2011, **47**, 2601–2603.
- Q. Dou and Y. Zhang, *Langmuir*, 2011, **27**, 13236.
- M. Wang, C. Mi, W. Wang, C. Liu, Y. Wu, Z. Xu, C. Mao and S. Xu, *ACS Nano*, 2009, **3**, 1580.
- E. Downing, L. Hesselink, J. Ralston and R. Macfarlane, *Science*, 1996, **273**, 1185.
- A. Shalav, B. S. Richard, T. Trupke, K. W. Kramer and H. U. Gudel, *Appl. Phys. Lett.*, 2005, **86**, 013505.